# A New Method for Describing the Mechanism of a Chemical Reaction Based on the Unified Reaction Valley Approach

Wenli Zou, Thomas Sexton, Elfi Kraka, Marek Freindorf, and Dieter Cremer*

Computational and Theoretical Chemistry Group (CATCO), Department of Chemistry, Southern Methodist University, 3215 Daniel Ave, Dallas, Texas 75275-0314, United States

ABSTRACT: The unified reaction valley approach (URVA) used for a detailed mechanistic analysis of chemical reactions is improved in three different ways: (i) Direction and curvature of path are analyzed in terms of internal coordinate components that no longer depend on local vibrational modes. In this way, the path analysis is no longer sensitive to path instabilities associated with the occurrences of imaginary frequencies. (ii) The use of third order terms of the energy for a local description of the reaction valley allows an extension of the URVA analysis into the pre- and postchemical regions of the reaction path, which are typically characterized by flat energy regions. (iii) Configurational and conformational processes of the reaction complex are made transparent even in cases where these imply energy changes far less than a kcal/mol by exploiting the topology of the potential energy surface. As examples, the rhodium-catalyzed methanol carbonization, the Diels−Alder reaction between 1,3-butadiene and ethene, and the rearrangement of HCN to CNH are discussed.
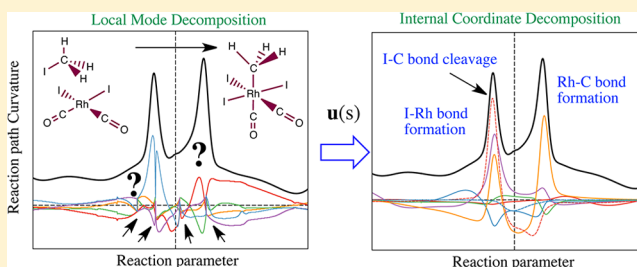
INTRODUCTION

Knowledge of the mechanism of a chemical reaction is a fundamental prerequisite for the control of chemical reactions and their manipulation to lead to useful, nondangerous materials. Nowadays, the study of the reaction mechanism is possible utilizing the advanced methodologies of quantum chemistry. Two important concepts are introduced in this connection: First, the Born−Oppenheimer approximation,[1] which leads to a separation of nuclear and electronic motion, is applied for the description of the reaction complex (RC) being the union of the reactants. Second, the reaction is described in a 3N−L dimensional model space (N: number of atoms of the RC; L: number of overall translations and rotations of the RC), which leads to the potential energy (hyper)surface (PES) spanned by the coordinates of the RC. Provided a sufficient amount of energy (E) is available, the RC moves from a low-E region up an E-valley to an E-pass point and then down through another E-valley to the E-minimum of the products. The path with the smallest E-increase and the lowest E-barrier normally follows the floor-line in the entrance valley and passes at the transition state (TS: first order saddle point on the PES) to the exit valley with the location of products. More complex reaction paths with one or more energy minima occupied by (an) intermediate(s) are also possible. Furthermore, a reaction path bifurcates at a bifurcation point, which is a minimum in one and a maximum in another orthogonal direction of the 3N−L dimensional PES.[2]

The majority of computational reaction studies are based on the concept of the PES and analyzes the mechanism by just focusing on the stationary points along the reaction path (minima of reactants and products as well as the TS). The unified reaction valley approach (URVA)[3−7] represents a viable alternative as it follows the entire reaction path from reactants to products. URVA is based on (i) the reaction path Hamiltonian of Miller, Handy, and Adams,[8] (ii) an efficient path-following algorithm, (iii) the description of the reaction valley in terms of the properties of the generalized harmonic vibrational modes of the RC, and (iv) their decomposition in terms of local vibrational modes.[9−11] The changes in the electronic structure of the RC are monitored point by point along the reaction path, however, in an indirect rather than direct fashion. Attempting to analyze the RC by changes in electron density, geometry, and other molecular properties would produce a flood of data, hindering the identification of the most important, reaction-decisive electronic structure changes. For isolation of the most important changes, URVA makes a paradigm shift from the analysis of the RC to an analysis of the reaction path and the surrounding valley.[4,5] The reaction path is given by a curved line $\tilde{\mathbf{x}}(s)$, where the 3N dimensional vector is composed of mass-weighted Cartesian coordinates $\tilde{x}_i(s)$ (the tilde indicates mass-weighting), and the parameter s gives the arc length of the reaction path according to[8,12]

$$ds^2 = d\mathbf{x}^{\dagger}\mathbf{M}\,d\mathbf{x} = d\tilde{x}^{\dagger}\,d\tilde{x} \qquad (1)$$

with $\mathbf{M}$ being the diagonal matrix of nuclear masses. The reaction path line can be described at each point s by a Frenet−Serret frame given by the path direction (tangent) vector $t(s)$, the curvature (normal) vector $\kappa(s)$, and higher normal vectors

$\mathbf{r}_m(s)$, where for short reaction paths only the two former vectors are normally interesting. For a given point s of the reaction path, the tangent vector $t(s)$ can be used to determine that coordinate of the RC, which dominates the direction of the reaction path. The vector $\kappa(s)$ describes the curving of the reaction path, which is a consequence of the electronic structure changes of the RC.[4,5,13−20]

The PES reflects the E-change of a given RC in dependence of the internal coordinates $q_n(s)$ used to describe it.[21,22] If this E-change would always be linear, reaction paths would be straight lines, and chemistry could be fully described using classical mechanics. However, electrons and nuclei are charged particles, and therefore, the potential energy has a $1/r$ (r: distance between electrons, nuclei, etc.) dependence according to Coulomb and exchange interactions, which lead to nonlinear, more abrupt changes in the electronic structure of the RC. Similar to the valleys in a mountain region, the reaction valley through the E-mountains of the PES is curved where the curvature reflects nonlinear changes in the electronic structure. This can be rationalized in the following way: any electronic structure change leads to a change in the normal mode vibrations of the RC. The normal mode eigenvectors change their direction in the 3N−L dimensional space and can be described by a component being orthogonal to the path and one being parallel to the path. The latter describes a translation of the RC along the path. The larger the component along the path is, the stronger is the coupling between the vibration and the translation as measured by the coupling coefficients $B_{\mu s}(s)$.[3,7,8] Under the impact of this coupling, the path curves where the curvature can be evaluated via the sum of the squares of the coupling coefficients $B_{\mu s}(s)$, which are therefore called curvature coupling coefficients. Consequently, the curvature of the reaction path reflects the electronic structure changes of the RC, which is the basis for the paradigm shift from RC to the reaction path. The basic procedure of URVA[3−5,7] is to determine the reaction path curvature and the associated curvature coupling coefficients and to identify those vibrational modes of the RC that couple with the translation of the RC along the path. Experience shows that the number of vibrational modes relevant in this regard is always much smaller than 3N−L.[4,5,13−20] Often, only a few vibrational modes at a given path position s contribute to the curving of the reaction path.

Hence, the question has to be posted how to relate changes in the curvature coupling coefficients to changes in the electronic structure of the RC. Previously, we have solved this problem by decomposing normal mode curvature coupling coefficients $B_{\mu s}(s)$ into local mode curvature coupling coefficients $A_{ns}^{\kappa}(s)$[3], where the local vibrational modes are based on the mass-decoupled Euler−Lagrange equations of Konkoli and Cremer[9,10] and the local equivalent of the Wilson equation of vibrational spectroscopy.[23,24] Each local mode $\mathbf{a}_n$ is related to an internal coordinate q_n, which drives the local mode.[9] Hence, the curvature coupling coefficients $A_{ns}^{\kappa}(s)$ identify those internal coordinates $q_n(s)$ that describe the geometrical changes of the RC caused by its electronic structure changes. Eighty years of molecular orbital theory[25] and 50 years of the analysis of the electron density distribution of molecules[26] have provided thorough insight into the relationship between electronic structure changes and changes in the internal coordinates of the molecular geometry.[27,28] Once those internal coordinates are identified that cause curving of the reaction path, the corresponding electronic structure changes of

the RC can be identified, and a detailed account of the reaction mechanism can be given.

Both the strength and the weakness of the URVA analysis are the generalized local vibrational modes $\mathbf{a}_n^g(s)$, which are utilized as appropriate tools to determine the electronic structure changes of the RC along the reaction path.[3] The local modes $\mathbf{a}_n^g(s)$ provide a detailed account on the reaction mechanism but fail if the description of the reaction path is hampered by path instabilities. Path instabilities can have different origins. (i) They appear when in the course of the bond forming or breaking processes the RC adopts a (bi)radicaloid electronic structure, which is insufficiently described by the single determinant method normally used for extensive reaction path calculations (including the calculation of RC geometries and frequencies at up to 2000 points along the reaction path). There might be other methodological shortcomings in the description of the RC, but the use of a single determinant approach for a multireference problem is the major cause for path instabilities. (ii) The latter can also have a chemical origin, such as when the reaction path bifurcates as an intrinsic feature of the PES of the RC. In all cases, the path instability is indicated by the occurrence of one or more imaginary frequencies, which suggest the existence of side-valleys and the conversion of the reaction path from a path along the floor line of a valley to a ridge path between two or more side-valleys. Sometimes the E-changes between ridge path and side-valley paths are small, and the ridge path can still be considered as a representative reaction path.

However, any path instability precludes the description of electronic structure changes in terms of local mode curvature coupling coefficients $A_{n,s}^{\kappa}(s)$. In this situation, it is desirable to identify and describe electronic structure changes of the RC by a robust alternative method that is not sensitive to path instabilities. Furthermore, we will show that the description of the reaction path can be improved so that it can be followed far out into the van der Waals regions of reactants and products. In the van der Waals region of the RC, curvature peaks are small, and therefore, we will present a technique as to how a useful analysis can be carried out in such a case.

Results of this work will be presented in the following way. In section 2 the most important features of URVA will be summarized so that, in section 3, a new method of describing electronic structure changes of the RC along the reaction path can be presented. In section 4, the implementation and the computational details of the new method are summarized.

■ BASIC METHODOLOGY OF URVA

In (3N−L) dimensional space, the reaction path is a curved line, which is conveniently described by the path direction and the path curvature in the form of suitable Frenet vectors. The reaction path direction at a path point s is given by the unit vector $\boldsymbol{\eta}(s)$[3]

$$\boldsymbol{\eta}(s) = \frac{d\tilde{\mathbf{x}}(s)}{ds} = -\frac{\tilde{\mathbf{g}}(\tilde{\mathbf{x}}(s))}{c(s)} \qquad (2)$$

where the derivative of the mass-weighted reaction coordinate $\tilde{\mathbf{x}}(s)$ with regard to s is the normalized mass-weighted gradient vector $\tilde{\mathbf{g}}(s)/c(s)$ with the normalization constant $c(s)$ being equal to the length $\|\tilde{\mathbf{g}}(s)\|$ of the gradient vector. In URVA, the direction vector $\boldsymbol{\eta}(s)$ is analyzed in terms of internal coordinate basis vectors $\mathbf{u}(s)$ according to[3]

$$\boldsymbol{\eta}(s) = \sum_{n=1}^{3N-L} t_n \mathbf{u}_n(s) \tag{3}$$

with

$$\mathbf{u}_n = \frac{\mathbf{M}^{-1/2}\mathbf{b}_n^{\dagger}}{\|\mathbf{M}^{-1/2}\mathbf{b}_n^{\dagger}\|} = G_{n,n}^{-1/2}(\mathbf{M}^{-1/2}\mathbf{b}_n^{\dagger}) \tag{4}$$

where $\mathbf{b}_n$ is a row vector of the $\mathbf{B}$-matrix with elements $\partial q_n/\partial x_i$, and $G_{n,n}$ is a diagonal element of the kinetic energy matrix $\mathbf{G}$.[29] It is noteworthy that the unit vector $\mathbf{u}_n(s)$ can point in any direction of the $3N-L$ dimensional space, and therefore, its component (anti)parallel to $\boldsymbol{\eta}(s)$ has to be projected out, which leads to the amplitudes t_n.

The curvature vector $\boldsymbol{\kappa}(s)$ is given by[3,12]

$$\boldsymbol{\kappa}(s) = \frac{d^2\tilde{\mathbf{x}}(s)}{ds^2} = \frac{d\boldsymbol{\eta}(s)}{ds}$$
$$= \frac{-1}{\|\tilde{\mathbf{g}}(s)\|}(\tilde{\mathbf{f}}^x(s)\boldsymbol{\eta}(s) - [(\boldsymbol{\eta}(s))^{\dagger}\tilde{\mathbf{f}}^x(s)\boldsymbol{\eta}(s)]\boldsymbol{\eta}(s)) \tag{5}$$

Here, matrix $\tilde{\mathbf{f}}^x(s)$ is the mass-weighted force constants matrix expressed in Cartesian coordinates. All vibrational properties have to be expressed with the help of mass-weighted generalized normal vibrational modes $\tilde{\mathbf{g}}(s)$ defined in a $3N-L-1$-dimensional subspace, which one obtains by determining the force constant matrix $(\tilde{\mathbf{f}}^x)^g(s)$ in the subspace with the help of a suitable projection operator $\mathbf{P}(s)$[12]

$$(\tilde{\mathbf{f}}^x)^g(s) = (\mathbf{I} - \mathbf{P}(s))\tilde{\mathbf{f}}^x(s)(\mathbf{I} - \mathbf{P}(s)) \tag{6}$$

so that the generalized mass-weighted vibrational modes can be determined by solving a generalized Wilson equation[12,29]

$$\tilde{\mathbf{f}}^g(s)\tilde{l}_{\mu}^g(s) = (2\pi c\omega_{\mu}^g(s))^2\tilde{l}_{\mu}^g(s) \tag{7}$$

with $\omega_{\mu}^g(s)$ being the generalized vibrational frequencies and constant c the speed of light. The curvature coupling coefficients $B_{\mu s}(s)$ are related to the curvature vector by eq 8.

$$B_{\mu s}(s) = \boldsymbol{\kappa}(s)^{\dagger}\tilde{l}_{\mu}^g(s) \tag{8}$$

and the scalar curvature $\kappa(s) = \|\boldsymbol{\kappa}(s)\|$ is given by[8]

$$\kappa(s) = \left[\sum_{\mu}^{3N-L-1} B_{\mu s}^2(s)\right]^{1/2} \tag{9}$$

Direction and curvature of the reaction path are decomposed in terms of the amplitudes A_{ns}^{η} and A_{ns}^{κ}

$$A_{ns}^{\eta}(s) = \frac{(\tilde{\mathbf{g}}(s)^{\dagger}\tilde{\mathbf{b}}_n(s)^{\dagger})^2}{(\tilde{\mathbf{g}}(s)^{\dagger}\tilde{\mathbf{g}}(s))(\tilde{\mathbf{b}}_n(s)\tilde{\mathbf{b}}_n(s)^{\dagger})} \tag{10}$$

$$A_{ns}^{\kappa}(s) = \frac{\boldsymbol{\kappa}(s)^{\dagger}\mathbf{a}_n^g(s)}{\sqrt{((\mathbf{a}_n^g(s))^{\dagger}\mathbf{a}_n^g(s))}} \tag{11}$$

with $\tilde{\mathbf{b}}_n(s) = \mathbf{M}^{-1/2}\mathbf{b}_n(s)$, $\tilde{\mathbf{g}}(s) = \mathbf{M}^{-1/2}\mathbf{g}(s) = -c(s)\boldsymbol{\eta}(s)$, and t_n of eq 3 being

$$t_n = (A_{ns}^{\eta}(s))^{1/2} \tag{12}$$

In Figure 1, a typical path instability is shown for the precursor step of the Rh-catalyzed methanol carbonylation.[30] In regions I and II, the vibrational frequency $\omega_1^g(s)$ becomes imaginary as indicated in Figure 1 by a negative frequency value. This leads to problems when decomposing the reaction
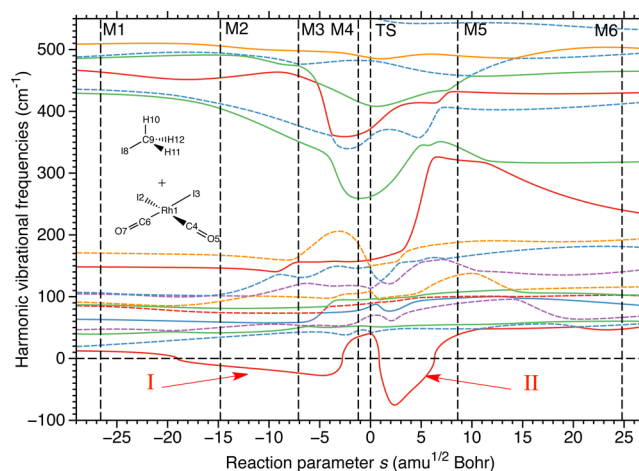

Figure 1. Calculated $3N-7$ vibrational frequencies of the reaction complex (RC) of the precursor step of the Rh-catalyzed methanol carbonylation as a function of the reaction path parameter s. Regions I and II (lowest frequency given in red) denote path instabilities as indicated by the occurrence of imaginary frequencies (given as negative values). B3LYP/6-31G(d,p)/SDD calculations.

path curvature into local mode curvature coupling coefficients $A_{ns}^{\kappa}(s)$, as is shown in Figure 2. In regions I and II, the $A_{ns}^{\kappa}(s)$
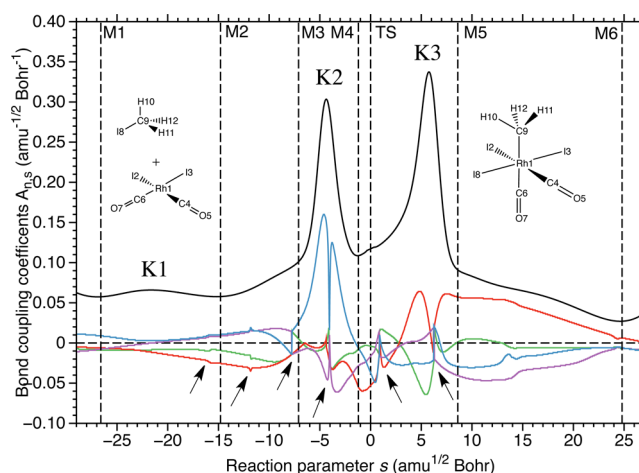

Figure 2. Scalar reaction path curvature (black line) of the precursor step of the Rh-catalyzed methanol carbonylation as a function of the reaction path parameter s. The decomposition of the curvature into local mode curvature coupling coefficients fails (as indicated by the black arrows) because they are not defined in regions with imaginary frequencies. Curvature peaks K2 and K3 cannot be explained. B3LYP/6-31G(d,p)/SDD calculations.

curves have smaller and larger spikes (indicated by black arrows). It is not possible to identify any generalized local mode that is associated with the curvature peak K2 or K3 via large local curvature coupling coefficients $A_{ns}^{\kappa}(s)$ caused by a coupling between translational and local vibrational modes. The local mode concept requires $3N-L-1$ real positive normal-mode frequencies and fails if one or more of them become imaginary.[3] Hence, the $A_{ns}^{\kappa}(s)$ in regions I and II do not have any physical meaning.

There are different possibilities to solve the problem of the imaginary generalized frequencies in regions I and II: (i) One can extend the theory of the reaction path Hamiltonian to that of a reaction surface Hamiltonian[31,32] and only the $3N-L-(n$

+1) generalized vibrational modes (n indicating the number of additional imaginary frequencies) orthogonal to the reaction surface are used in the analysis. This is in principle possible;[6] however, it makes the analysis too costly and will only be appropriate if the chemical processes in question justify the use of a reaction surface. (ii) Alternatively, one could use a low-cost multireference method to eliminate path instabilities. This would be a reasonable solution to the problem, but aside from CASSCF,[33,34] there is hardly any other method that (a) can be used with analytical first and second E-derivatives and (b) is economically suitable for extended reaction path investigations. CASSCF is adding nondynamical electron correlation effects but lacks the important dynamical correlation effects and, in this regard, has similar deficits as the Hartree–Fock method. In light of this, it is desirable to use DFT methods that are either combined with CASSCF[35−37] or based on XC functionals including multireference effects.[38] Future developmental work will clarify whether, in this way, the path instability problem of URVA can be efficiently solved. (iii) There are scattered cases for which the extension from a nonredundant coordinate set to a redundant coordinate set for the description of the RC helps to suppress path instabilities,[39] which is in line with the improved convergence of geometry optimizations when carried out with a redundant set of coordinates.[40−42] Atoms move during a molecular motion (reactions or large amplitude motions) on curved paths, which are mimicked by redundant sets of rectangular coordinates (Cartesian or internal coordinates). It would be better to use curvilinear coordinates.[43,44] Zou and Cremer[45−47] have already demonstrated the advantages of using curvilinear coordinates in the case of ring rearrangements. However, a generally applicable method of describing chemical reactions in terms of curvilinear coordinates is still missing.[48−50]

Possibilities i−iii are only of limited value, especially if they make URVA dependent on costly methods that cannot be generally applied. A generally applicable and robust method, which is independent of any path instabilities, is more attractive. Therefore, we will describe such a method in the following.

■ DECOMPOSITION OF THE PATH DIRECTION AND CURVATURE INTO INTERNAL COORDINATE COMPONENTS

In this work, URVA was extended for the use of redundant internal coordinates as a basis for a more efficient path following and analyzing method. This led to a reduction of the time needed for the constrained optimization of the geometry of the RC at a given path point but did not lead to a general elimination of path instabilities. Noteworthy in this connection is the fact that the analysis of vectors $\boldsymbol{\eta}(s)$ and $\boldsymbol{\kappa}(s)$ has to be carried out in a 3N−L dimensional space and therefore requires the conversion from a redundant to a nonredundant coordinate set before the URVA analysis is carried out.[40]

In light of the limited practicality of possibilities, a new decomposition of vectors $\boldsymbol{\eta}(s)$ and $\boldsymbol{\kappa}(s)$ was worked out, which is based on internal coordinate basis vectors as a suitable alternative to local vibrational mode vectors.

Components of the Path Direction. The partitioning of the path direction vector $\boldsymbol{\eta}(s)$ into internal coordinate components can be based on eqs 3 and 4.[3] Accordingly, the component for internal coordinate q_n is given by

$$\eta_n^q(s) = \frac{\mathrm{d}\tilde{q}_n(s)}{\mathrm{d}s} = G_{n,n}^{-1/2}(\mathbf{M}^{-1/2}\mathbf{b}_n^\dagger(s))^\dagger \boldsymbol{\eta}(s) \tag{13}$$

$$= \mathbf{u}_n^\dagger(s)\boldsymbol{\eta}(s) \tag{14}$$

$$= \cos \alpha_n(s) \tag{15}$$

because $\|\boldsymbol{\eta}(s)\| \equiv 1$ and $\mathbf{u}_n(s)$ are also unit vectors. The generalized angle α_n gives the deviation of internal coordinate vector $\mathbf{u}_n(s)$ from the direction defined by the vector $\boldsymbol{\eta}(s)$ in 3N−L dimensional space. Eq 15 indicates that $\eta_n^q(s)$ is obtained by the projection of $\mathbf{u}_n$ onto the reaction path vector $\boldsymbol{\eta}$.

It is obvious that amplitudes $A_{\eta,s}^n(s)$ and $\eta_n^q(s)$ are related by eq 16.

$$A_{n,s}^\eta(s) = \frac{(\tilde{\mathbf{g}}^\dagger(s)\tilde{\mathbf{b}}_n(s)^\dagger)^2}{(\tilde{\mathbf{g}}^\dagger(s)\tilde{\mathbf{g}}(s))(\tilde{\mathbf{b}}_n(s)\tilde{\mathbf{b}}_n(s)^\dagger)} = (\mathbf{u}_n^\dagger(s)\boldsymbol{\eta}(s))^2 = (\eta_n^q(s))^2 \tag{16}$$

i.e., the previously used amplitude $A_{\eta,s}^n(s)$ is always positive and accordingly misses important sign information. The sign of the component $\eta_n^q(s)$ contributing to $\boldsymbol{\eta}(s)$ reveals whether the associated internal coordinate mode supports (positive sign) or resists (negative sign) the motion of the RC along the reaction path. If $\cos \alpha_n(s)$ becomes negative for $90 < \alpha < 180°$, the local internal coordinate vector $\mathbf{u}_n(s)$ can be split into a contribution being antiparallel and one being perpendicular to the path, where the latter is typical of normal vibrational modes not interacting with the translational motion of the RC. The part that is antiparallel to the path direction indicates a local translational mode that resists the reactive motion along the path. Hence, it is useful to replace amplitude $A_{\eta,s}^n(s)$ of the previous version of URVA[3] by amplitude $\eta_n^q(s)$.

Components of the Path Curvature. Because the local curvature coupling coefficients fail to present the correct mechanism in areas of path instabilities, the internal coordinate components of the scalar curvature are derived here by following the procedure applied for the decomposition of the path tangent vector utilizing internal coordinate basis vectors $\mathbf{u}_n(s)$.

$$\frac{\mathrm{d}^2\tilde{q}_n(s)}{\mathrm{d}s^2} = \frac{\mathrm{d}\eta_n^q(s)}{\mathrm{d}s}$$
$$= G_{n,n}^{-1/2}(\mathbf{b}_n(s)\mathbf{M}^{-1/2})\boldsymbol{\kappa}(s) + G_{n,n}^{-1/2}(\boldsymbol{\eta}^\dagger(s)\mathbf{M}^{-1/2}$$
$$\mathrm{d}\mathbf{b}_n(s)\mathbf{M}^{-1/2})\boldsymbol{\eta}(s)$$
$$= \mathbf{u}_n^\dagger(s)\cdot\boldsymbol{\kappa}(s) + \frac{\mathrm{d}\mathbf{u}_n^\dagger(s)}{\mathrm{d}s}\cdot\boldsymbol{\eta}(s) \tag{17}$$

$$= \|\boldsymbol{\kappa}(s)\|\cos \beta_n(s) + \left\|\frac{\mathrm{d}\mathbf{u}_n(s)}{\mathrm{d}s}\right\|\cos \gamma_n(s) = \kappa_n^q(s) + \eta_n^u(s) \tag{18}$$

where $\mathrm{d}\mathbf{b}_n(s)$ is the differential of vector $\mathbf{b}_n(s)$ with regard to s, $\beta_n(s)$ is the generalized angle between vectors $\boldsymbol{\kappa}(s)$ and $\mathbf{u}_n(s)$, and $\gamma_n(s)$ is the corresponding angle between $\boldsymbol{\eta}(s)$ and $\mathrm{d}\mathbf{u}_n(s)/\mathrm{d}s$. The first term on the r.h.s. of eq 18 is the projection of $\mathbf{u}_n(s)$ onto the curvature vector $\boldsymbol{\kappa}(s)$ leading to the amplitude $\|\mathbf{u}_n(s)\|\cos \beta_n(s) = \cos \beta_n(s) = \kappa_n^q(s)$, as each $\mathbf{u}_n$ is a unit vector describing the local motion, which is driven by the internal coordinate $q_n(s)$. The amplitude is scaled by the scalar curvature $\|\boldsymbol{\kappa}(s)\|$ corresponding to the length of the curvature vector in 3N−L dimensional space.

The mixed second order term $\eta_n^u(s)$ is determined by the change in the direction of $\mathbf{u}_n(s)$ with s and the tangent vector. The vector derivative $d\mathbf{u}_n(s)/ds$ that is orthogonal to $\mathbf{u}_n(s)$ is projected onto vector $\boldsymbol{\eta}$ and therefore does not have any information on the curvature. Because of the components $\eta_n^u(s)$, the quantity $\|\sum_n(d^2\tilde{q}_n(s)/ds^2)\|$ can be larger than $\|\kappa(s)\|$, i.e., the second derivatives $d^2\tilde{q}_n(s)/ds^2$ are contaminated by the mixed second order contributions relevant in connection with the reaction path direction rather than its curvature. Hence, the curvature contribution of the internal coordinate $q_{n(s)}$ is defined by the first term of eq 18

$$\kappa_n^q(s) = G_{n,n}^{-1/2}(\mathbf{b}_n(s)\mathbf{M}^{-1/2})\kappa(s) = \kappa^\dagger(s)\mathbf{u}_n(s) \qquad (19)$$

It is useful to relate the curvature component $\kappa_n^q(s)$ to the local curvature coupling coefficient $A_{n,s}^\kappa(s)$.[3] For this purpose, the coefficient $A_{ns}^\kappa(s)$ of eq 11 is rewritten in a form that connects to eq 17

$$A_{n,s}^\kappa(s) = \kappa^\dagger(s)\mathbf{v}_n(s) \qquad (20)$$

where the generalized local mode unit vector $\mathbf{v}_n(s)$ is defined by

$$\mathbf{v}_n(s) = \frac{\tilde{\mathbf{a}}_n^g(s)}{\|\tilde{\mathbf{a}}_n^g(s)\|} \qquad (21)$$

$$\tilde{\mathbf{a}}_n^g(s) = \mathbf{M}^{1/2}\mathbf{L}(s)\mathbf{a}_n(s) \qquad (22)$$

$$\mathbf{a}_n(s) = \frac{\mathbf{K}^{-1}(s)\mathbf{d}_n^\dagger(s)}{\mathbf{d}_n(s)\mathbf{K}^{-1}(s)\mathbf{d}_n^\dagger(s)} = k_n^a(s)\mathbf{K}^{-1}(s)\mathbf{L}^\dagger(s)\mathbf{b}_n^\dagger(s) \qquad (23)$$

Here, $\mathbf{L}(s)$ collects all generalized normal mode vectors $\tilde{\mathbf{l}}_\mu^g(s)$ of eq 7, $\mathbf{K}(s)$ is the diagonalized force constant matrix, $\mathbf{d}_n(s)$ is a row vector of the internal coordinate equivalent of $\mathbf{L}(s)$, $\mathbf{D}(s)$, and $k_n^a(s)$ is the local mode force constants associated with $\mathbf{a}_n(s)$. The normalized local mode vector $\mathbf{v}_n(s)$ can be written as

$$\mathbf{v}_n(s) = \frac{k_n^a(s)}{\|\tilde{\mathbf{a}}_n^g(s)\|}\mathbf{M}^{1/2}\mathbf{L}(s)\mathbf{K}^{-1}(s)\mathbf{L}^\dagger(s)\mathbf{M}^{1/2}(\mathbf{M}^{-1/2}\mathbf{b}_n^\dagger(s)) \qquad (24)$$

$$= \frac{k_n^a(s)G_{n,n}^{1/2}}{\|\tilde{\mathbf{a}}_n^g(s)\|}(\mathbf{M}^{1/2}\mathbf{L}(s)\mathbf{K}^{-1}(s)\mathbf{L}^\dagger(s)\mathbf{M}^{1/2})\mathbf{u}_n(s) \qquad (25)$$

$$= p_n(s)(\tilde{\mathbf{f}}^x(s))^{\{-1\}}\mathbf{u}_n(s) \qquad (26)$$

where

$$p_n(s) = \frac{k_n^a(s)G_{n,n}^{1/2}}{\|\tilde{\mathbf{a}}_n^g(s)\|}$$

$$= \frac{1}{\sqrt{\mathbf{u}_n^\dagger(s)(\tilde{\mathbf{f}}^x(s))^{\{-2\}}\mathbf{u}_n(s)}} \qquad (27)$$

The symbols $\{-1\}$ and $\{-2\}$ denote the generalized inverses of the corresponding matrices. Utilizing eq 26, eq 20 reads

$$A_{n,s}^\kappa(s) = p_n(s)\kappa^\dagger(s)(\tilde{\mathbf{f}}^x(s))^{\{-1\}}\mathbf{u}_n(s) = p_n(s)\kappa^\dagger(s)\boldsymbol{\Gamma}(s)\mathbf{u}_n(s) \qquad (28)$$

which, by utilizing the compliance matrix $\boldsymbol{\Gamma}(s)$ as the inverse of the force constant matrix,[23,51] can be related to eq 19. Obviously, the curvature vector can be analyzed using different sets of internal coordinate unit vectors. Inspection reveals that curvature coupling coefficients $A_{n,s}^\kappa(s)$ in eq 20 and internal

coordinate components $\kappa_n^q(s)$ in eq 19 have similar shape in the absence of path instabilities. Advantages and disadvantages of these two sets have to be discussed in the following.

Implementation and Computational Details. The component analysis of tangent vector $\boldsymbol{\eta}(s)$ and curvature vector $\boldsymbol{\kappa}(s)$ was programmed and implemented into the program package COLOGNE2015.[52] It was tested for a precursor step of the Rh-catalyzed methanol carbonylation (see Figure 2), the HCN rearrangement to CNH, and the Diels−Alder reaction between 1,3-butadiene and ethene (see the following). In all URVA calculations, a path increment of $\Delta s = 0.03$ amu$^{1/2}$ Bohr (abbreviated in the text by s-units or path units for reasons of simplification) was used in connection with tight SCF (changes in the density matrix $\leq 10^{-8}$) and tight geometry optimization criteria (changes in the root-mean-square (RMS) force being $\leq 10^{-6}$ atomic units) and an RMS displacement $\leq 4 \times 10^{-6}$ Bohr. For the corrector step of the path following algorithm, the Bulerich−Stoer integrator[53] was used with a convergence criterion of 10^{-8}.

The investigation of the Diels−Alder reaction was carried out with the density functional theory (DFT) hybrid functional B3LYP[54,55] employing the 6-31G(d,p) basis set[56] (activation energy $\Delta E^a = 23.4$ kcal/mol and reaction energy $\Delta_R E = -41.2$ kcal/mol). In the case of the Rh-catalyzed reaction the SDD (Stuttgart−Dresden) effective core potential[57] was added for Rh, thus leading to a B3LYP/6-31G(d,p)/SDD description ($\Delta E^a = 40.2$ kcal/mol; $\Delta_R E = -2.5$ kcal/mol). The HCN rearrangement was studied at the MP2 (second order Møller−Plesset perturbation theory[58,59]) level of theory using the 6-31G(d,p) basis ($\Delta E^a = 55.1$ kcal/mol; $\Delta_R E = 20.1$ kcal/mol). In each case, the energetics was checked for the reactions in question by CCSD(T)[60] calculations in the sense of a dual level approach (relatively low accuracy for calculating the features of reaction path and reaction valley; relatively high accuracy for determining the energetics of the reaction). These were single point CCSD(T) calculations with DFT geometries and a cc-pVDZ/SDD basis set[61] for the Rh-catalyzed reaction ($\Delta E^a = 38.1$ kcal/mol; $\Delta_R E = -10.3$ kcal/mol), CCSD(T)/CBS (complete basis set) calculations based on Dunning's cc-pVQZ, cc-pV5Z, and cc-pV6Z basis sets,[62,63] optimized geometries ($\Delta E^a = 44.7$ kcal/mol; $\Delta_R E = 14.9$ kcal/mol) for the HCN rearrangement, and CCSD(T) single point calculations with a cc-pVQZ basis set[62] at DFT geometries for the Diels−Alder reaction ($\Delta E^a = 22.4$ kcal/mol; $\Delta_R E = -44.9$ kcal/mol).

Different grids were used in the DFT calculations. Preliminary calculations were always done with a normal fine (NF) grid of (75, 302) points (number of radial shells, number of angular points per shell; in total, 22650 grid points per atom). For the Diels−Alder reaction, the accuracy of the DFT calculations was improved by using an ultrafine grid of (99, 590) points (in total 58410 points per atom) and a superfine (SF) grid of (150, 974) points for first and second period elements (146100 points) and (225, 974) points. For all third and higher period elements, a (225, 974) grid was used (Rh: 219150 points).[64,65] The URVA calculations were carried out with the program package COLOGNE2015.[52] For the CCSD(T) calculations, the programs MOLPRO[66] and CFOUR[67] were used, whereas the DFT calculations were carried out with Gaussian09.[68]

Testing the Component Analysis of the Reaction Path Curvature. Use of the internal coordinate basis vectors and the curvature components $\kappa_n^q(s)$ leads to a solution of the path

instability problem shown in Figure 2, which is documented in Figure 3 (curvature: solid black line; components: colored
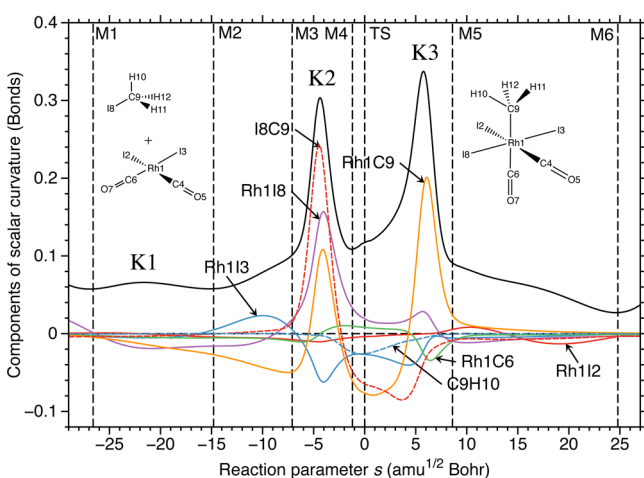

Figure 3. Scalar reaction path curvature (black line) of the precursor step of the Rh-catalyzed methanol carbonylation is decomposed into internal coordinate components where all are given as a function of the reaction path parameter s. The decomposition performs correctly in regions of path instability (Figure 1). Curvature peaks K1, K2, and K3 can now be analyzed and explained.

lines). The component analysis of the curvature in terms of $\kappa_n^q(s)$ contributions reveals that curvature peaks K1, K2, and K3 are associated with the breaking of the C9I8 bond (K2), the forming of the Rh1I8 bond (K1 and K2), and the forming of the Rh1C9 bond (K2 and K3). The change from negative (resisting the curving of the reaction path) to positive curvature contributions (supporting the curving) gives a detailed description of electronic structure changes in the RC along the reaction path, which is accompanied by small changes in the RhI3, RhI2, and RhC6 bonds.

Contributions $\kappa_n^q(s)$ and $\eta_n^u(s)$ of eq 18 are compared in Figure 4. Figure 4a shows, as a solid black line, the Cartesian scalar curvature $\kappa^x(s)$, which is analytically calculated in Cartesian coordinate space according to eq 5 and therefore represents the most reliable ("exact") curvature function. The internal coordinate curvature

$$\kappa^q(s) = \left[\sum_{n=1}^{3N-L} (\kappa_n^q(s))^2 \right]^{1/2} \tag{29}$$

is based on the contributions resulting from the internal coordinate basis vectors $\mathbf{u}_n$ in the direction of the curvature vector $\boldsymbol{\kappa}^x(s)$ in $3N-L$ dimensional space. Contrary to the local mode vectors $\mathbf{a}_n$, the basis vectors $\mathbf{u}_n$ are not derived from a dynamic principle (the Euler–Lagrange equations in the case of $\mathbf{a}_n$[9]) and therefore contain contributions from kinematic coupling as becomes obvious when comparing the norms of $\boldsymbol{\kappa}^x(s)$ and $\boldsymbol{\kappa}^q(s)$, where the latter is given by

$$\|\boldsymbol{\kappa}^q(s)\|^2 = (\boldsymbol{\kappa}^x(s))^\dagger \mathbf{U}(s)\mathbf{U}^\dagger(s)\boldsymbol{\kappa}^x(s)$$
$$= (\boldsymbol{\kappa}^x(s))^\dagger (\mathbf{M}^{-1/2}\mathbf{B}^\dagger(s)\mathbf{G}_{n,n}^{-1}(s)\mathbf{B}(s)\mathbf{M}^{-1/2})\boldsymbol{\kappa}^x(s) \tag{30}$$

because $\boldsymbol{\kappa}^q(s) = \mathbf{U}^\dagger(s)\boldsymbol{\kappa}^x(s)$ and matrix $\mathbf{U}(s) = \mathbf{M}^{-1/2} \mathbf{B}^\dagger(s) \mathbf{G}_{n,n}^{-1}(s)$ collects the basis vectors $\mathbf{u}_n(s)$ of eq 4. The requirement $\|\boldsymbol{\kappa}^q(s)\|^2 = \|\boldsymbol{\kappa}^x(s)\|^2$ can only be fulfilled if $\mathbf{B}^\dagger(s)\mathbf{G}_{n,n}^{-1}(s)\mathbf{B}(s) = \mathbf{M}$, which is not possible because (i) the off-diagonal elements
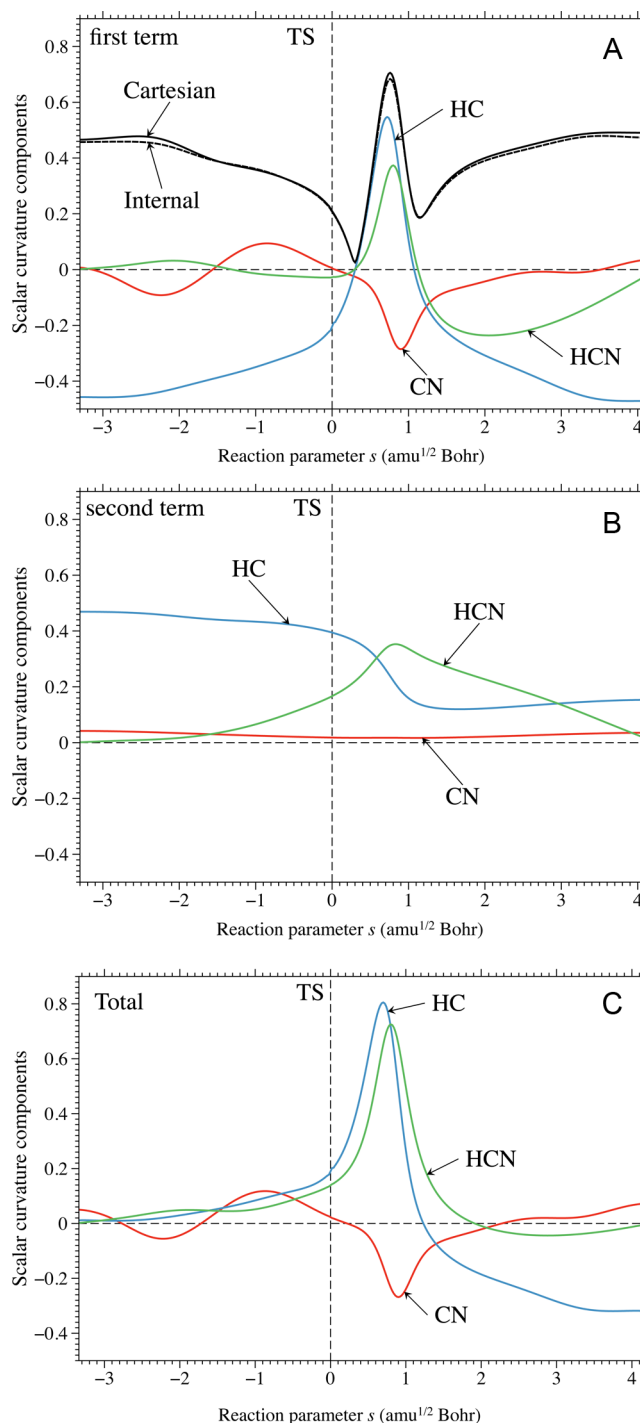

Figure 4. Decomposition of the curvature of the reaction path into internal coordinate components (distances HC and CN; angle HCN) for the rearrangement of HCN to CNH. (a) First term of eq 17. (b) Second term of eq 17. (c) Sum of first and second terms of eq 17 (MP2/6-31G(d,p) calculations).

of $\mathbf{G}$ are missing and (ii) $\mathbf{B}^\dagger(s)\mathbf{G}^{-1}(s)\mathbf{B}(s) = \mathbf{B}^\dagger(s)(\mathbf{B}(s) \mathbf{M}^{-1}\mathbf{B}^\dagger(s))^{-1}\mathbf{B}$ does not lead to $\mathbf{M}$ in light of the fact that the rectangular matrix $\mathbf{B}$ ($3N \times (3N-L)$) has no inverse.

One could augment matrix $\mathbf{B}$ by including L rotations and translation so that a square ($3N \times 3N$) matrix $\mathbf{A}$ results, which has an inverse, so that

$$\mathbf{A}^\dagger(s)(\mathbf{A}(s)\mathbf{M}^{-1}\mathbf{A}^\dagger(s))^{-1}\mathbf{A} = \mathbf{M} \tag{31}$$

results, which would give $\|\boldsymbol{\kappa}^q(s)\|^2 = \|\boldsymbol{\kappa}^x(s)\|^2$ but would imply an undesired coupling between vibrations, translations, and rotations at path positions where the gradient does not vanish. Hence, $\|\boldsymbol{\kappa}^q(s)\|^2 \neq \|\boldsymbol{\kappa}^x(s)\|^2$ in light of a kinematic coupling of the basis vectors $\mathbf{u}_n$ (representing local internal coordinate modes) via the diagonal elements of the $\mathbf{G}$ matrix.

For insight into the magnitude of errors resulting from kinematic coupling of the $\mathbf{u}_n$, the difference $\Delta\kappa(s) = \kappa^x(s) - \kappa^q(s)$ can be plotted, or the two scalar curvatures can be directly compared as in Figure 4a (solid black line: $\kappa^x(s)$; dashed black line: $\kappa^q(s)$). Overall, differences are small and seem to become slightly larger for large $\|s\|$ values. In general, we make the observation that, with an increasing number of $\kappa_n^q(s)$ contributions to the internal coordinate curvature, differences become larger or, alternatively, increase with the magnitude of the diagonal elements of $\mathbf{G}$.

In Figure 4a–c, the internal coordinate terms $\kappa_n^q(s)$, $\eta_n^u(s)$, and their sum corresponding to $d^2\tilde{q}_n(s)/ds^2$ (see eq 17) are plotted as a function of s for the rearrangement of HCN to CNH. The reaction path is defined in a 3-dimensional space that can be spanned by the distances HC and CN as well as the bending angle HCN, where the latter two could be replaced by the redundant parameters NH and HNC. The corresponding internal coordinate components are shown in Figure 4 by a blue (HC), red (CN), and green (HCN) line. Any deviation from the linear HCN (CNH) form leads to immediate electronic structure changes as a result of σ, π-mixing and bond length changes. Therefore, curvature values are relatively large at the start and the end of the reaction path, which is correctly reflected by the negative contribution $\kappa_{HC}^q(s)$. According to eq 29, this contribution must be squared and then will dominate the positive curvature. The sum of the HC contributions $\kappa_n^q(s)$ and $\eta_n^u(s)$ is close to zero as local mode HC also contributes to the direction of the reaction path (Figure 4b) so that the second HC term of eq 17 becomes positive and thereby cancels the first term. The HCN rearrangement proceeds via a cyclic, nonclassical structure (partial 2e-3c bonding) located after the TS, which is responsible for the curvature peak at 0.9 s-units to which all internal coordinate modes contribute.

The CN-contribution is almost the same for $\kappa_n^q(s)$ and the total value of $d^2\tilde{q}_n(s)/ds^2$ (see eq 17), which is a result of the fact that $\eta_{CN}^u(s)$ has little influence on the reaction path direction $\boldsymbol{\eta}(s)$, thus leading to a small second term contribution throughout the whole reaction path (Figure 4b). The HCN bending contributions are closely connected with the HC (or NH) bond length changes and complement them. It is noteworthy that the HC distance is, toward the end of the reaction, no longer a meaningful parameter, as the HC bond is broken and electronic structure changes now concern the NH distance. This is another example of a reaction that is better described in curvilinear rather than rectangular coordinates.[47] Apart from this, the component analysis provides a detailed insight into the electronic structure changes of the RC in the HCN → CNH rearrangement and also gives details on the path contributions $\eta_n^u(s)$ as well as the kinematic coupling between the $\mathbf{u}_n(s)$ modes.

■ FOLLOWING THE REACTION PATH INTO THE VAN DER WAALS REGION

Previous work with URVA was exclusively aimed at the investigation of the chemical region of a reaction path (region of electronic structure changes in connection with bond breaking and bond forming).[18−20] In the pre- and postchemical regions, i.e., in the van der Waals regions of entrance and exit channel, E-changes and therefore electronic structure changes of the RC are small. They include configurational changes in the RC caused by a change in the van der Waals interactions between the reaction partners and conformational changes of one of the reactants where both processes are often characterized by charge polarization and charge transfer in the millielectron (me) range. Therefore, the URVA investigation of the van der Waals range seemed likely to be a waste of computer time as it was doubtful whether it would lead to any useful mechanistic insight or would even produce more than numerical noise in the path properties to be calculated. This is corroborated by the URVA analysis of conformational processes of isolated molecules, such as the internal rotation of ethane, the inversion of cyclohexane, the pseudorotation of cyclopentane, or the rotation at the central bond of 1,3-butadiene (see below), which only lead to negligible curvature changes.

Two important developments have changed these expectations: (i) a new path-following algorithm developed by Hrant and Kraka[69] to get more accurate curvature values for rearrangement reactions, and (ii) increased understanding of the handling of path branching points in URVA investigations. Originally, the first development was not intended for an extended analysis of the pre- and postchemical processes but will be adjusted for this very purpose in the following.

Standard Euler Predictor Corrector and Hessian-based Predictor-Corrector methods, which are routinely used for reaction path following,[70−73] are not accurate far out in the entrance or exit channel, i.e., in regions where the PES is relatively flat. Hence, the length of the E-gradient as well as its components become very small, which according to eq 5 will lead to erratic curvature values when the reaction valley and its floor-line are not accurately described.

Predictor-corrector (PC) integrators are composed of three steps: (i) the predictor integration step (P), (ii) one or more function evaluation steps (E), and (iii) the corrector step (C).[74] After some P and E steps, the PES and its derivative(s) in this region are evaluated, a local surface is fitted by applying distance weighted interpolants (DWI),[75] and then an accurate C step is performed. Both Euler and Hessian-based PC algorithms lead to the same numerical problems when describing shallow reaction valleys. Because they only share the DWI surface fitting procedure, it is obvious that the problem is caused by deficiencies in the DWI-fitted surfaces. These surfaces are defined as weighted linear combinations of Taylor series expansions T_{i-1} and T_i about the previous and current P end points $\tilde{\mathbf{x}}_{i-1}$ and $\tilde{\mathbf{x}}_i$.

$$E_{DWI}(\tilde{\mathbf{x}}) = \omega_{i-1}(\tilde{\mathbf{x}})T_{i-1}(\tilde{\mathbf{x}}) + \omega_i(\tilde{\mathbf{x}})T_i(\tilde{\mathbf{x}}) \tag{32}$$

with the weighing functions $\omega_{i-1}(\tilde{\mathbf{x}})$ and $\omega_i(\tilde{\mathbf{x}})$ for the P end points. Previous implementations used simplified weighting functions of the form $\|\Delta\tilde{\mathbf{x}}\|^{-2}$ and a Taylor series expansion up to second order given according to[70−72]

$$T_{i-1}(\tilde{\mathbf{x}}) = E_{i-1} + \tilde{\mathbf{g}}_{i-1}^\dagger\Delta\tilde{\mathbf{x}}_{i-1} + \frac{1}{2}\Delta\tilde{\mathbf{x}}_{i-1}^\dagger\mathbf{f}_{i-1}^x\Delta\tilde{\mathbf{x}}_{i-1} \tag{33}$$

$$T_i(\tilde{\mathbf{x}}) = E_i + \tilde{\mathbf{g}}_i^\dagger\Delta\tilde{\mathbf{x}}_i + \frac{1}{2}\Delta\tilde{\mathbf{x}}_i^\dagger\mathbf{f}_i^x\Delta\tilde{\mathbf{x}}_i \tag{34}$$

It is known that a DWI surface becomes exact to nth order if (i) the primitive weighting functions decay as $\|\Delta\tilde{\mathbf{x}}\|^{-(n+1)}$ and (ii)
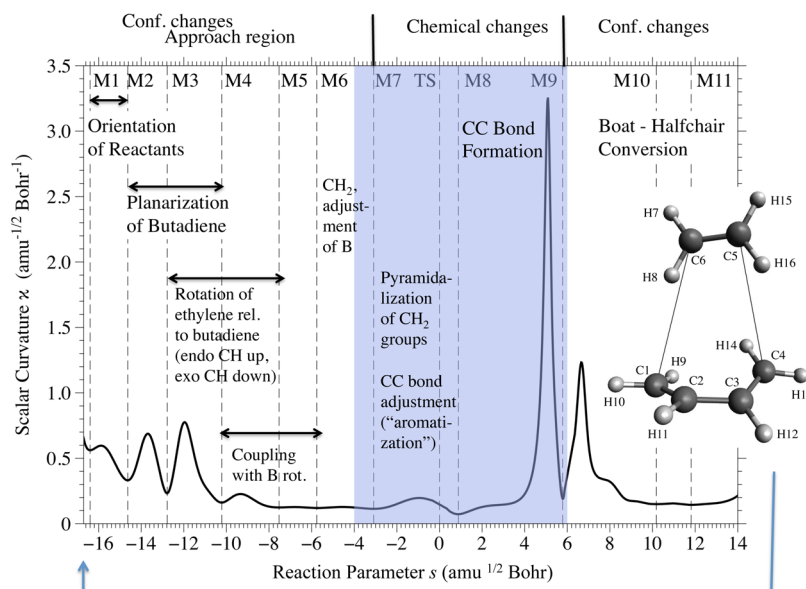
Figure 5. Curvature diagram of the Diels−Alder reaction between butadiene and ethylene. The colored region from −4 to 6 s-units is the region of chemical changes, which represented the range that could be analyzed with the previous reaction path following algorithm. The range from −17 to 14 s-units can now be investigated with the improved path-following algorithm.

the Taylor expansions include up to nth order contributions.[76] For the description of the reaction path in a flat reaction valley region, the standard Euler PC and Hessian-based PC algorithms must be extended to allow primitive weighting functions of the general form $\|\Delta\tilde{\mathbf{x}}\|^{-m}$ ($m = 4$ turns out to be sufficient to guarantee third order accuracy) and to include third-order terms in the Taylor expansion on the line between $\tilde{\mathbf{x}}_{i-1}$ and $\tilde{\mathbf{x}}_i$ defined by[69]

$$T_{i-1}(\tilde{\mathbf{x}}) = E_{i-1} + \tilde{\mathbf{g}}_{i-1}^{\dagger}\Delta\tilde{\mathbf{x}}_{i-1} + \frac{1}{2}\Delta\tilde{\mathbf{x}}_{i-1}^{\dagger}\mathbf{f}_{i-1}^{x}\Delta\tilde{\mathbf{x}}_{i-1}$$
$$+ \frac{1}{6}(\Delta\tilde{\mathbf{x}}_{i-1}^{\dagger}\mathbf{p})\Delta\tilde{\mathbf{x}}_{i-1}^{\dagger}\mathbf{P}\Delta\tilde{\mathbf{x}}_{i-1} \qquad (35)$$

$$T_i(\tilde{\mathbf{x}}) = E_i + \tilde{\mathbf{g}}_i^{\dagger}\Delta\tilde{\mathbf{x}}_i + \frac{1}{2}\Delta\tilde{\mathbf{x}}_i^{\dagger}\mathbf{f}_i^{x}\Delta\tilde{\mathbf{x}}_i + \frac{1}{6}(\Delta\tilde{\mathbf{x}}_i^{\dagger}\mathbf{p})\Delta\tilde{\mathbf{x}}_i^{\dagger}\mathbf{P}\Delta\tilde{\mathbf{x}}_i$$
$$(36)$$

where the matrix $\mathbf{P}$ is given by

$$\mathbf{P} = \frac{1}{\|\tilde{\mathbf{x}}_i - \tilde{\mathbf{x}}_{i-1}\|}(\tilde{\mathbf{f}}_i^{x} - \tilde{\mathbf{f}}_{i-1}^{x}) \qquad (37)$$

and the unit vector $\mathbf{p}$ is defined as

$$\mathbf{p} = \frac{\tilde{\mathbf{x}}_i - \tilde{\mathbf{x}}_{i-1}}{\|\tilde{\mathbf{x}}_i - \tilde{\mathbf{x}}_{i-1}\|} \qquad (38)$$

This simplification avoids the calculation of the full set of third derivatives and therefore is cost-effective.[69] The resulting enhanced Euler-PC and Hessian-based PC integrators do not require considerably more computational time or memory than their predecessors but make it possible to follow the reaction path far out into the entrance or exit channel of a chemical reaction, thus providing the possibility of analyzing pre- and postchemical processes.

In Figure 5, the investigation of the Diels−Alder reaction between 1,3-butadiene and ethene is shown as an example. With the previous algorithm,[3] this reaction could only be investigated in the range from −4 to 6 s-units.[18] However, with the new algorithm described above, the path range of the

URVA analysis is increased by 300% to the range of −17 to 14 s-units and still makes it possible to calculate $\kappa(s)$ and other path (valley) properties with sufficient accuracy (see Figure 5). For example, in the prechemical region, four curvature peaks are visible, which are associated with a rotation of ethene ("orientation of reactants", Figure 5) that leads to a H···π-bonded van der Waals complex. Next, two "planarization peaks" are visible, which correspond to a planarization of the gauche form of 1,3-butadiene. The C_s-symmetrical form of the RC is adopted via an additional rotation and sideways movement of ethene.

The postchemical region starts at $s = 6$ units and is characterized by a relatively large curvature peak with a shoulder ($7 < s < 8$ s-units). Up to the end of the reaction path at $s = 14$ units, there are just relatively small curvature enhancements associated with the ring-pseudorotation of cyclohexene from a boat form into the more stable half-chair form.[44] The curvature peaks in the pre- and postchemical region are all relatively large and easy to identify, which is a contradiction with the fact that conformational processes never lead to pronounced curvature peaks. This finding has to be explained in the next section.

■ IMPACT OF BIFURCATION POINTS ON THE CURVATURE OF THE REACTION PATH

The current URVA algorithm is set up such that it starts at the first order saddle point of the PES and then follows the downhill paths to the closest minimum in entrance and exit channel. Therefore, we will explore the reaction valley and the topology of the PES in the entrance channel of the Diels−Alder reaction by following the downhill path as it would have to be taken for the retro-Diels−Alder reaction. A bifurcation point (BIFP) toward the end of this path is indicated at −6.5 s-units by a valley ridge inflection point (VRIP) at which the lowest vibrational frequency, $\omega_1^g(s)$, becomes zero and then, beyond the VRIP, adopts an imaginary value. Two side-valleys emerge, which enclose the reaction path as a ridge path. In high accuracy calculations (very small step size and tight

convergence criteria for the constrained geometry optimization at each path point), the ridge path is followed by the RC up to the BIFP in line with the McIver—Stanton rules,[77,78] according to which the RC can change its symmetry only at a stationary point (TS or BIFP). Once the BIFP is reached, the RC adopts C_1 symmetry, and the prechemical steps of the Diels—Alder reaction take place. These are discussed in the following for the retro-Diels—Alder reaction, i.e., from the BIFP down to one of the side-valleys and then out into the van der Waals region where the reactants depart.

Analysis of the Prechemical Events: The Optimal Situation. Once the major electronic structure changes of the RC are finished, the diene adopts its more stable gauche form, which causes the ethene to rotate out of the coaligned, almost coplanar form into an RC configuration where two of the ethene H atoms in cis-position are attracted by the π-density of the diene double bonds (C−H···π interactions). Note that here and in the following, we distinguish the conformational changes of one part of the RC from the configurational changes, which describe the relative arrangement of the reactants to each other. In Figure 6(a), the rotation of free gauche 1,3-butadiene (local minimum) into its cis-form (TS of the gauche—gauche rotation; relative energy of the TS: 0.34 kcal/mol) is analyzed utilizing the curvature of the rotation path. A similar analysis is carried out in Figure 6(b) for the prechemical movement of the RC down from the BIFP to the van der Waals region. The scalar curvature in Figure 6(a) is typical of a conformational process with marginal electronic structure changes: The curvature values are all ≤0.4 κ-units. From the TS on the right side of diagram, there is a constant curvature of 0.18 κ-units up to ±1.5 s-units, which increases when reaching the gauche form (in Figure 6(a) at $s = -1.9$ units on the far left). Relaxation in the CCC bending angles and CC bond length changes are responsible for this. Also, the CCCC torsional angle, which determines the path direction (in the sense of a rotation) at the TS makes a contribution for the gauche form. We conclude that conformational processes, even if they involve changes in steric strain, make only negligible contributions to the curvature of the reaction path.

This is totally different when the butadiene rotates from the cis to the gauche form within the RC when interacting with the ethene reactant (Figure 6(a)). The curvature diagram is almost the same from the TS on (only the path leading to the entrance channel is analyzed in Figure 6(a); the BIFP is equal to the TS of this process as shown on the far right) up to $s = -1.5$ units. Then, the curvature raises to a large peak of 4.1 κ-units positioned at $s = -1.9$ units. Major components of this curvature peak are the C1C2C3C4 dihedral angle of 1,3-butadiene indicating that the rotation into the gauche form is almost completed, and a new path direction is adopted. Because the path tangent $\boldsymbol{\eta}(s)$ (determining the path direction) and path curvature vector $\boldsymbol{\kappa}(s)$ are orthogonal in (3N−6) dimensional space, an internal coordinate component contributing strongly to $\boldsymbol{\eta}(s)$ can only make a small contribution to $\boldsymbol{\kappa}(s)$ and vice versa. The component analysis of the path direction (Figure 7) reveals, in the range $-1.7 \geq s \geq 2.0$ units, a change from the internal coordinates describing the cis-gauche rotation of 1,3-butadiene to those describing a rotation of the ethene plane into a position where it includes a 50° angle with the averaged C1C2C3C4 plane of the diene.

There is no change in the charge transfer at the curvature peak (4 me are transferred from ethene to 1,3-butadiene). However, there is a significant change in the polarization of the
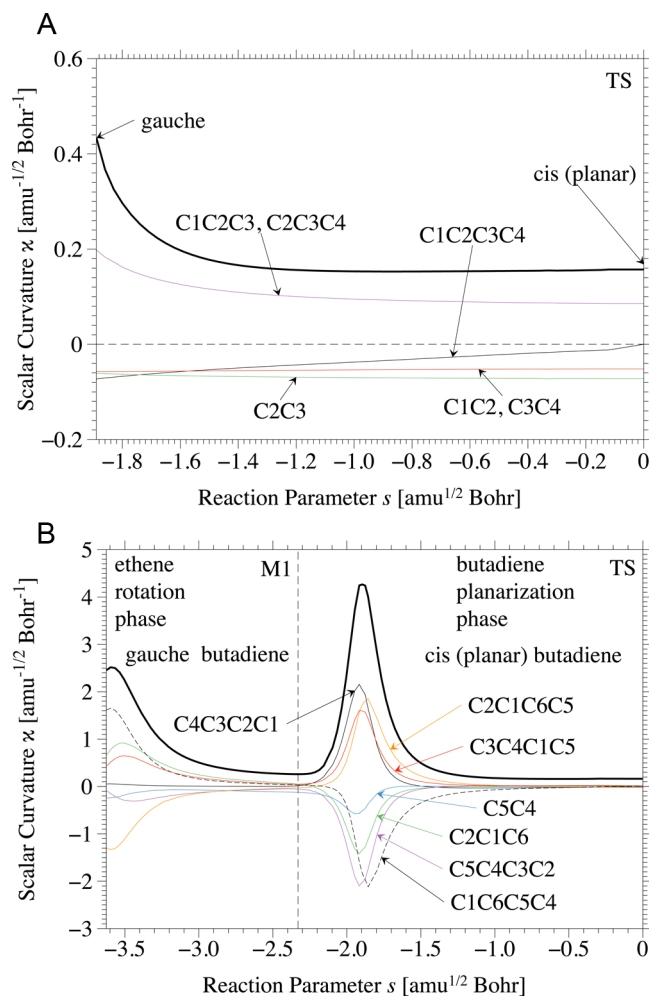

Figure 6. (a) Scalar curvature (bold line) and curvature components (thin lines) for the gauche-cis rotation of free 1,3-butadiene where the planar C_s-symmetrical cis form is located at the TS and only the entrance channel of the gauche—gauche rotation is given. (b) Scalar curvature (bold line) and curvature components (thin lines) for the gauche-cis rotation of 1,3-butadiene located within the RC of the Diels—Alder reaction with ethene. M1 denotes a curvature minimum, which separates the ethene rotation phase from the butadiene planarization phase. The RC has C_1-symmetry and adopts C_s-symmetry at the TS, which is a BIFP of the Diels—Alder reaction (see text). For the numbering of atoms, see Figure 5 (B3LYP/6-31G(d,p) calculations with a UF grid).

latter in the way that the C1H$_2$ and C2H groups become more negatively charged than C3H and C4H$_2$ with a complementary polarization of the ethene CH$_2$ groups. From $s = -2.1$ on, the path into the van der Waals region is dominated by orientation angles such as C1C6C5C4 or C2C1C6C5, which position the ethene group so that it is stabilized via (C−)H···π interactions within the RC where ethene is the donor of these weak nonclassical H-bonds. We conclude that changes in the path direction of the RC are clearly indicated by curvature peaks, although the corresponding electronic structure changes are small. The E-changes for a decrease in s from 0 to −3.7 units by just 0.34 kcal/mol, which is a tiny change compared to the activation energy of the Diels—Alder reaction (23.4 kcal/mol, see above). Nevertheless, the curvature as a third-order response property sensitively registers any change in the
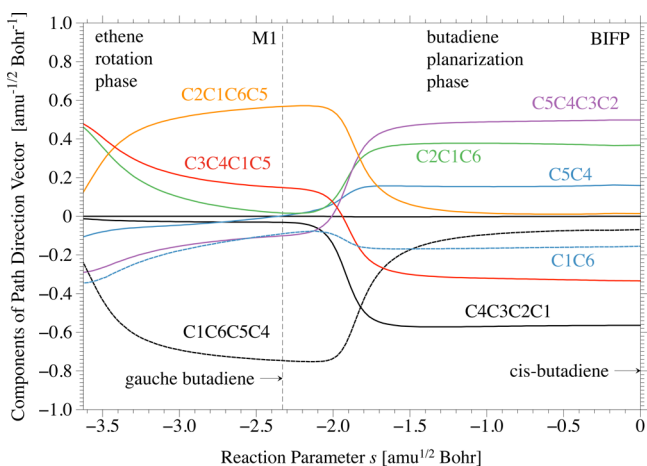
Figure 7. Components of the unit direction vector $\eta(s)$ for the gauche-cis rotation of 1,3-butadiene located within the RC of the Diels–Alder reaction with ethene. M1 denotes a curvature minimum, which separates the ethene rotation phase from the butadiene planarization phase. The RC has C_1-symmetry and adopts C_s-symmetry at the TS, which is a BIFP (bifurcation point) of the Diels–Alder reaction (see text). For the numbering of atoms, see Figure 5 (B3LYP/6-31G(d,p) calculations with a UF grid).

Figure 8. Scalar curvature $\kappa(s)$ shown in the entrance channel of the Diels−Alder reaction between 1,3-butadiene and ethene. The B3LYP/6-31G(d,p) calculations were carried out with the normal fine (NF) grid (red line), an ultrafine (UF) grid (blue line), and a superfine (SF) grid (green line). Distinct points (P1, ···, P5) along the reaction path are indicated. See text.

reaction path and therefore accurately registers configurational exchanges in the RC.

Analysis of the Prechemical Events: The Real Situation. In routine studies with the URVA program, the exact position of VRIPs and/or BIFPs is not directly determined. As a matter of fact, the step-size used when following the reaction path makes it unlikely to determine a VRIP correctly. For the same reason, the ridge path is seldom followed up to the BIFP. It is more likely that the RC leaves the ridge path in a downhill journey into one of the side valleys. This departure from the ridge path assists the URVA analysis as it amplifies curvature changes connected with relatively small electronic structure changes. Additional reaction path investigations down from a BIFP to a side valley, as done in this work, are time-consuming but provide no more information than the investigation of a path only partly following the ridge before curving down to a side valley to follow the valley floor to an energy minimum in the entrance channel.

The correct analysis of such a path in the pre(post)-chemical processes requires an understanding of the topology of the PES in this region so that the meaning of each curvature peak can be clarified. In Figure 8, the curvature of the reaction path is shown in the entrance channel of the Diels−Alder reaction for different accuracies of the DFT calculation used in this case: NF (normal fine) grid (red line in Figure 8), UF (ultrafine) grid (blue line), and SF (super fine) grid (green line). Depending to what grid is used in the DFT calculations, different scalar curvatures are obtained for $s \leq -6.73$ units ($s = -6.73$ units: position of the VRIP). The changes in the scalar curvature are small in the vicinity of the VRIP when NF and UF grids are used but become significant toward -18 units where both calculations stop. When using an SF grid, the differences are substantial (all curvature peaks are moved by approximately 3 s-units into the van der Waals region and are significantly higher), and the path does not stop before -19.7 units. Obviously, the new path-following algorithm in connection with tight convergence criteria for the geometry optimization and an SF grid for the DFT calculations is the most reliable
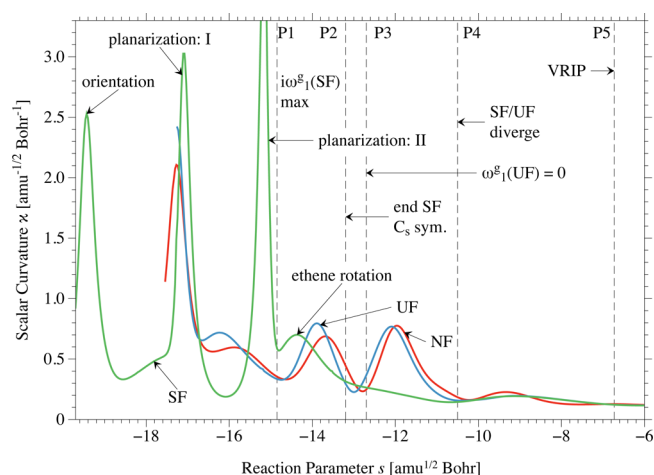
when exploring the reaction path far out into the entrance channel. However, the question has to be answered: What is the nature of the path taken?

This can be specified with the help of the calculated low-range frequencies (Figure 9), the E-changes (Figure 10(a)),
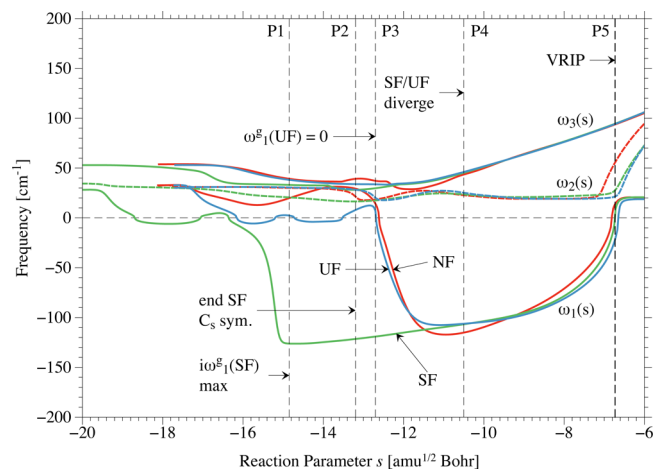

Figure 9. Normal mode frequencies $\omega_1(s)$, $\omega_2(s)$, and $\omega_3(s)$ are shown in the entrance channel of the Diels−Alder reaction between 1,3-butadiene and ethene. Imaginary frequencies are given as negative frequencies. The B3LYP/6-31G(d,p) calculations were carried out with an ultrafine (UF) grid (blue line) and a superfine (SF) grid (green line). Distinct points (P1, ···, P5) along the reaction path are indicated so that the comparison with Figure 8 is facilitated; see text.

and the changes in the C1C2C3C4 dihedral angle of the diene unit (Figure 10(b)). After the VRIP (point P5 in all diagrams), the 3 DFT calculations follow the ridge path up to approximately P4, where UF- and SF-path (in the following, short for "the path calculated with a UF grid") diverge shortly after the NF path departs from them (Figure 8). There are now two rather than just one curvature peak associated with the cis-gauche rotation of 1,3-butadiene (curvature component analysis not shown). The frequency diagram reveals that, after P5 up to P4, the RC follows the ridge path, although the ridge becomes a
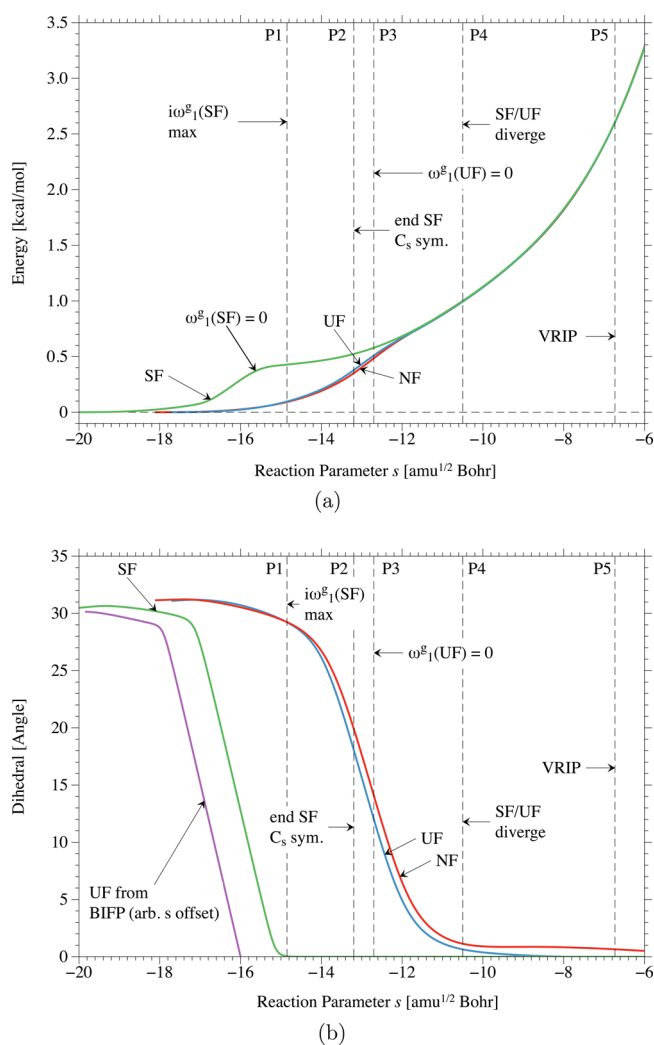
Figure 10. (a) Change of the energy along the path of the Diels–Alder reaction between 1,3-butadiene and ethene in the entrance channel of the reaction. Reference is the BSSE-corrected energy of the separated reactants. The B3LYP/6-31G(d,p) calculations were carried out with an ultrafine (UF) grid (blue line) and a superfine (SF) grid (green line). Distinct points (P1, ⋯, P5) along the reaction path are indicated so that the comparison with Figure 8 is facilitated. (b) Change in the dihedral angle C1C2C3C4(s) of 1,3-butadiene when being part of the RC of the Diels–Alder reaction with ethene. Colors and points Pn as in (a). The dihedral angle C1C2C3C4(s) for the path from bifurcation point BIFP down to a side-valley is included for reasons of comparison, where an arbitrary s offset is used. For the numbering of atoms, see Figure 5.

more and more pronounced maximum between two increasingly deeper side-valleys as indicated by the increase in the value of the imaginary frequency ω_1 (indicated in Figure 9 by a more negative value of ω_1). At P4, the magnitude of the imaginary frequency ω_1(UF) begins to decrease, indicating that the RC takes a path down from the ridge into one of the side valleys, which implies a curving of the analyzed reaction path (blue curvature peak at −12 s-units, Figure 8), a change of the RC from C_s to C_1 symmetry, a decrease in the energy by 0.5 kcal/mol (Figure 10(a)), and rotation of the diene into its gauche form (C1C2C3C4 dihedral angle: 31°; Figure 10(b)).

When the UF-RC approaches the floor-line of the side valley, $i\omega_1$(UF) (Figure 9) becomes real and positive (point P3), and the downhill path curves into the direction of the side valley,

which causes the second curvature peak in connection with the diene cis-gauche rotation (curving of the blue dihedral angle line in Figure 10(b) to a limit value of 31°). This curvature peak corresponds to the "planarization" peak for the path down from the BIFP in Figure 6(b) and has as its cause a change in the path direction from a diene-rotation in the RC to an ethene rotation as described above. Hence, it becomes obvious that conformational changes of the RC taking place in the prechemical range are made visible because of the topology of the PES (a ridge path between emerging side-valleys) acting like a curvature amplifier.

If the RC follows the ridge path farther out into the entrance channel as in the case for the SF-description, $i\omega_1$ continues to become larger beyond P4 up to P1 (Figure 9) as the side-valleys become deeper and the lateral decline of the ridge path steeper. Already at P2, the accuracy of the SF calculation is no longer sufficient to exactly keep the C_s symmetry of the RC. First slowly, but from P1 on abruptly, the SF path curves down the ridge into the side valley similarly to the UF or NF paths, only now the curvature peaks are much larger (green curvature line in Figure 9). The more accurate the description, the longer the RC follows the ridge path, and the more abrupt is the down-curving of the path as reflected by the large "planarization" peaks. This is confirmed by a much steeper increase of the C1C2C3C4 dihedral angle from P1 in (Figure 10(b)).

Noteworthy in this connection is the fact that the E-change is just 0.4 kcal/mol from P1 to the end of the reaction path at −19.7 path units (Figure 10(a)). Clearly, the energy is not sensitive enough to reveal details such as small configurational or conformational changes in the RC and their influence on the reaction mechanism. Mechanistic details become obvious when analyzing the curvature, which as a third order response property registers all changes in the electronic structure of the RC. However, so far these were always limited to the range of the chemical changes. This is the first time the curvature is used to describe prechemical events.

A BIFP of the Diels–Alder reaction is also located close to s = 6 units in the exit channel of the reaction (Figure 5). A relatively large curvature peak is found at 6.5 units, which can be identified as a curving of the path leading to cyclohexene in its half-boat form into the pseudorotation path, which the RC follows to convert into the more stable half-chair form.[44] Once ring pseudorotation has started, there are relatively small conformational changes of the RC, which do not show up in the curvature of the remaining path up to 14 path units (Figure 5).

■ CONCLUSIONS

The URVA method for determining the sequence of electronic structure changes, which an RC undergoes in the course of a chemical reaction, depends strongly on (i) the analysis of the direction of the reaction path vector $\eta(s)$ and the scalar curvature $\kappa(s)$ of the reaction path, (ii) the extent to which the reaction path can be followed into the pre- and postchemical regions, and (iii) the amplification of small electronic structure changes in connection with configurational and conformational processes of the RC in the van der Waals region. For all three requirements, substantial improvements could be reached in this work.

(1) The analysis of direction and curvature of the reaction path, previously performed in terms of local vibrational modes,[3] has been replaced by a component analysis of $\eta(s)$ and $\kappa(s)$ in

terms of local internal coordinate mode vectors $\mathbf{u}_n$ and the amplitudes $\eta_n^q(s)$ and $\kappa_n^q(s)$, respectively, which can be directly related to the electronic structure changes taking place in the RC when moving along the reaction path.

(2) The analysis of the scalar curvature in terms of $\kappa_n^q(s)$ components, introduced in this work, has been proven to be robust with regard to path instabilities and makes a meaningful analysis of the curvature possible in all parts of the reaction path (compare Figures 2 and 3).

(3) A disadvantage of the $\kappa_n^q(s)$ components is that they are based on local internal coordinate mode vectors $\mathbf{u}_n$, which are, contrary to the local modes $\mathbf{a}_n$,[9] still kinematically coupled via the diagonal elements of the $\mathbf{G}$-matrix as they have not been derived from a dynamic principle. However, this "disadvantage" of the $\mathbf{u}_n$ makes the new method of analyzing the path curvature insensitive to any path instability. Comparison of $\kappa^q(s)$ that is calculated from $3N-L$ components $\kappa_n^q(s)$ with the exact curvature $\kappa^x(s)$ reveals that differences because of coupling errors are relatively small and can be ignored in an analysis of the reaction mechanism.

(4) The URVA method was improved by installing a procedure recently suggested by Hrant and Kraka[69] to improve the reaction path and reaction curvature description of rearrangement reactions, which have a well-defined path length. The improvement is based on the introduction of third order terms in the predictor-corrector method used. In this way, the previously analyzed path region of the Diels−Alder reaction between 1,3-butadiene and ethene has been enlarged by more than 300% from 10 to 31 s-units thus including, besides the chemical region of the bond breaking/forming processes, also the prechemical (13 s-units) and postchemical (8 s-units) regions. This is a general observation for bimolecular reactions, whereas in the case of unimolecular reactions, the improved description of the fuction $\kappa(s)$ can be confirmed.[69] In the case of the Diels−Alder reaction, configurational changes of the RC involving the mutual orientation of the reactants (ethene rotation and gauche-butadiene planarization) in the entrance channel and pseudorotation of cyclohexene in the exit channel can now be analyzed, which was not previously possible.[18]

(5) One of the major advantages of URVA is that the mechanistic analysis can be carried out with any representative path. This can be exploited in the pre- and postchemical regions of the reaction path, which are often characterized by path bifurcations indicative of configurational or conformational processes of the RC. As a BIFP is mostly preceded by a VRIP and a ridge path flanked by side-valleys,[2] the accuracy of the applied path following method leads sooner or later to a curving down from the ridge path to the floor-line of one of the side-valleys. In this way, curvature peaks are generated, which amplify configurational or conformational changes of the RC (the more accurate the path-following method, the later the curving down and the larger the curvature peak). As shown in this work, one can choose the grid of a DFT calculation to enlarge the magnitude of the curvature peaks. Because the URVA analysis can be carried out for any path being a combination of ridge following, downhill, and side-valley path, the conformational changes of the RC can be analyzed once the topology of the PES is known in the region of the analysis. The latter can be extracted from the properties of the generalized normal-mode frequencies $\omega_\mu^g(s)$, the curvature $\kappa(s)$, the path direction components $\eta_n^q(s)$, characteristic internal coordinates $q_n(s)$, and the energy $E(s)$ calculated under different conditions as demonstrated in this work.

(6) The curvature analysis of conformational processes of the RC in the pre- and postchemical regions of the reaction path should provide little information as changes in $\kappa(s)$ are small. A change in the reaction path caused by the topology of the PES acts like an amplifier of the $\kappa(s)$ changes and makes URVA analysis of the pre- and postchemical ranges of the reaction path meaningful.

(7) The URVA method was extended in such a way that the RC can be described with a redundant set of internal coordinates. However, for the analysis of the path direction and curvature, nonredundant sets of $(3N-L)$ internal coordinates have to be used. A test was installed according to which it is clarified whether the internal coordinates chosen properly span the $(3N-L)$ dimensional space.

The realization of the component analysis of the path curvature and path direction in terms of internal coordinates is a major breakthrough for the URVA analysis of any (simple or complicated) chemical reaction. Currently, a major investigation of 90 homogeneous catalysis reactions is carried out utilizing the new method.

■ **AUTHOR INFORMATION**

Corresponding Author

*E-mail: dcremer@smu.edu.

Notes

The authors declare no competing financial interest.

■ **REFERENCES**

(1) Born, M.; Oppenheimer, J. R. On the Quantum Theory of Molecules (in German). *Ann. Phys.* **1927**, *389*, 457−484.

(2) Ess, D. H.; Wheeler, S. E.; Iafe, R. G.; Xu, L.; Celebi-Olcum, N.; Houk, K. N. Bifurcations on Potential Energy Surfaces of Organic Reactions. *Angew. Chem., Int. Ed.* **2008**, *47*, 7592−7601.

(3) Konkoli, Z.; Cremer, D.; Kraka, E. Unified Reaction Valley Approach: Mechanism of the Reaction CH$_3$ + H$_2$ → CH$_4$ + H. *J. Phys. Chem. A* **1997**, *101*, 1742−1757.

(4) Kraka, E.; Cremer, D. Computational Analysis of the Mechanism of Chemical Reactions in Terms of Reaction Phases: Hidden Intermediates and Hidden Transition State. *Acc. Chem. Res.* **2010**, *43*, 591−601.

(5) Cremer, D.; Kraka, E. From Molecular Vibrations to Bonding, Chemical Reactions, and Reaction Mechanism. *Curr. Org. Chem.* **2010**, *14*, 1524−1560.

(6) Kraka, E. In *Encyclopedia of Computational Chemistry*; Schleyer, P., Allinger, N., Clark, T., Gasteiger, J., Kollman, P., Schaefer, H., III, Schreiner, P., Eds.; Wiley: Chichester, 1998; Vol. 4; p 2437.

(7) Kraka, E. Reaction Path Hamiltonian and the Unified Reaction Valley Approach. *WIREs Comput. Mol. Sci.* **2011**, *1*, 531−556.

(8) Miller, W. H.; Handy, N. C.; Adams, J. E. Reaction path Hamiltonian for polyatomic molecules. *J. Chem. Phys.* **1980**, *72*, 99−112.

(9) Konkoli, Z.; Cremer, D. A New Way of Analyzing Vibrational Spectra I. Derivation of Adiabatic Internal Modes. *Int. J. Quantum Chem.* **1998**, *67*, 1−11.

(10) Konkoli, Z.; Cremer, D. A New Way of Analyzing Vibrational Spectra III. Characterization of Normal Vibrational Modes in Terms of Internal Vibrational Modes. *Int. J. Quantum Chem.* **1998**, *67*, 29−41.

(11) Kraka, E.; Larsson, J.; Cremer, D. In *Theoretical and Computational Chemistry, Vol. 5, Theoretical Organic Chemistry*; Parkanyi, C., Ed.; Elsevier: Amsterdam, 1998; p 259−327.

(12) Page, M.; McIver, J. W., Jr On evaluating the Reaction path Hamiltonian. *J. Chem. Phys.* **1988**, *88*, 922−935.

(13) Freindorf, M.; Sexton, T.; Kraka, E.; Cremer, D. The Mechanism of the Cycloaddition Reaction of 1.3-Dipole Molecules with Acetylene - An Investigation with the Unified Reaction Valley Approach. *Theor. Chem. Acc.* **2014**, *133*, 1423.1−1423.18.

(14) Kraka, E.; Zou, W.; Freindorf, M.; Cremer, D. Energetics and Mechanism of the Hydrogenation of XH_n for Group IV to Group VII Elements X. *J. Chem. Theory Comput.* **2012**, *8*, 4931−4943.

(15) Joo, H.; Kraka, E.; Quapp, W.; Cremer, D. The Mechanism of a Barrierless Reaction: Hidden Transition State and Hidden Intermediate in the Reaction of Methylene with Ethene. *Mol. Phys.* **2007**, *105*, 2697−2717.

(16) Kraka, E.; Joo, H.; Cremer, D. A stunning example for a spontaneous reaction with a complex mechanism: the vinylidene-acetylene cycloaddition reaction. *Mol. Phys.* **2010**, *108*, 2667−2685.

(17) Quapp, W.; Kraka, E.; Cremer, D. Finding the Transition State of Quasi-barrierless Reactions by a Growing String Method for Newton Trajectories: Application to the Dissociation of Methylenecyclopropene and Cyclopropane. *J. Phys. Chem. A* **2007**, *111*, 11287−11293.

(18) Kraka, E.; Wu, A.; Cremer, D. Mechanism of the Diels-Alder reaction studied with the united reaction valley approach: Mechanistic differences between symmetry-allowed and symmetry-forbidden reactions. *J. Phys. Chem. A* **2003**, *107*, 9008−9021.

(19) Kraka, E.; Cremer, D. Mechanism and dynamics of organic reactions: 1,2-H shift in methylchlorocarbene. *J. Phys. Org. Chem.* **2002**, *15*, 431−447.

(20) Cremer, D.; Wu, A.; Kraka, E. The mechanism of the reaction $FH + H_2C=CH_2 \rightarrow H_3C\text{-}CFH_2$. Investigation of hidden intermediates with the unified reaction valley approach. *Phys. Chem. Chem. Phys.* **2001**, *3*, 674−687.

(21) Dunning, T. H., Jr.; Harding, L. B.; Bair, R. A.; Eades, R. A.; Shepard, R. L. Theoretical Studies of the Energetics and Mechanisms of Chemical Reactions: Abstraction Reactions. *J. Phys. Chem.* **1986**, *90*, 344−356.

(22) Tao, P.; Sodt, A. J.; Shao, S. Y.; Konig, G.; Brooks, B. Computing the Free Energy along a Reaction Coordinate Using Rigid Body Dynamics. *J. Chem. Theory Comput.* **2014**, *10*, 4198−4207.

(23) Zou, W.; Kalescky, R.; Kraka, E.; Cremer, D. Relating Normal Vibrational Modes to Local Vibrational Modes with the help of an Adiabatic Connection Scheme. *J. Chem. Phys.* **2012**, *137*, 084114-1−11.

(24) Zou, W.; Kalescky, R.; Kraka, E.; Cremer, D. Relating normal vibrational modes to local vibrational modes benzene and naphthalene. *J. Chem. Phys.* **2012**, *137*, 1−13.

(25) Mulliken, R. S. Electronic Structures of Polyatomic Molecules and Valence. II. General Considerations. *Phys. Rev.* **1932**, *41*, 49−71.

(26) Bader, R. F. W. *Atoms in Molecules - A Quantum Theory*; Oxford University Press: Oxford, UK, 1990.

(27) Albright, T. A.; Burdett, J. K.; Whangbo, M.-H. *Orbital Interactions in Chemistry*; Wiley: New York, 2013.

(28) Weinhold, F.; Landis, C. R. *Valency and Bonding: A Natural Bond Orbital Donor-Acceptor Perspective*; Cambridge University Press: Cambrige, UK, 2003.

(29) Wilson, E. B.; Decius, J. C.; Cross, P. C. *Molecular Vibrations. The Theory of Infrared and Raman Vibrational Spectra*; McGraw-Hill: New York, 1955.

(30) Sparta, M.; Borve, K.; Jensen, V. Activity of Rhodium-catalyzed Hydroformylation: Added Insight and predictions from Theory. *J. Am. Chem. Soc.* **2007**, *129*, 8487−8499.

(31) Carrington, T., Jr; Miller, W. H. Reaction surface Hamiltonian for the dynamics of reactions in polyatomic systems. *J. Chem. Phys.* **1984**, *81*, 3942−3949.

(32) Carrington, T., Jr; Miller, W. H. Reaction surface description of intramolecular hydrogen atom transfer in malonaldehyde. *J. Chem. Phys.* **1986**, *84*, 4364−4370.

(33) Siegbahn, P.; Heiberg, A.; Roos, B.; Levy, B. Comparison of the Super-CI and the Newton-Raphson Scheme in the Complete Active Space SCF Method. *Phys. Scr.* **1980**, *21*, 323−327.

(34) Roos, B.; Taylor, P.; Siegbahn, P. A Complete Active Space SCF Method (CASSCF) Using a Density-matrix Formulated Super-CI Approach. *Chem. Phys.* **1980**, *48*, 157−173.

(35) Gräfenstein, J.; Cremer, D. The combination of density functional theory with multi- configuration methods - CAS-DFT. *Chem. Phys. Lett.* **2000**, *316*, 569−577.

(36) Cremer, D. Density functional theory: coverage of dynamic and non-dynamic electron correlation effects. *Mol. Phys.* **2001**, *99*, 1899−1940.

(37) Gräfenstein, J.; Cremer, D. Development of a CAS-DFT Method Accounting for Non-dynamical and Dynamical Electron Correlation in a Balanced Way. *Mol. Phys.* **2005**, *103*, 279−308.

(38) Becke, A. D. Density Functionals for Static, Dynamical, and Strong Correlation. *J. Chem. Phys.* **2013**, *138*, 074109.

(39) Chuang, Y.-Y.; Truhlar, D. G. Reaction-Path Dynamics in Redundant Internal Coordinates. *J. Phys. Chem. A* **1998**, *102*, 242−247.

(40) Bakken, V.; Helgaker, T. The efficient optimization of molecular geometries using redundant internal coordinates. *J. Chem. Phys.* **2002**, *117*, 9160−9174.

(41) Baker, J.; Kessi, A.; Delley, B. The generation and use of delocalized internal coordinates in geometry optimization. *J. Chem. Phys.* **1996**, *105*, 192−212.

(42) Pulay, P.; Fogarasi, G. Geometry optimization in redundant internal coordinates. *J. Chem. Phys.* **1992**, *96*, 2856−2860.

(43) Cremer, D.; Pople, J. A. A General Definition of Ring Puckering Coordinates. *J. Am. Chem. Soc.* **1975**, *97*, 1354−1358.

(44) Cremer, D.; Szabo, K. J. In *Methods in Stereochemical Analysis, Conformational Behavior of Six-Membered Rings, Analysis, Dynamics, and Stereoelectronic Effects*; Juaristi, E., Ed.; VCH Publishers, 1995; pp 59−134.

(45) Zou, W.; Izotov, D.; Cremer, D. New Way of Describing Static and Dynamic Deformations of the Jahn-Teller Type in Ring Molecules. *J. Phys. Chem. A* **2011**, *115*, 8731−8742.

(46) Zou, W.; Filatov, M.; Cremer, D. Bondpseudorotation, Jahn-Teller, and Pseudo-Jahn-Teller Effects in the Cyclopentadienyl Cation and its Pentahalogeno Derivatives. *Int. J. Quantum Chem.* **2012**, *112*, 3277−3288.

(47) Zou, W.; Cremer, D. Description of Bond Pseudorotation, Bond Pseudolibration, and Ring Pseudoinversion Processes caused by the Pseudo-Jahn-Teller Effect: Fluoro-Derivatives of the Cyclopropane Radical Cation. *Aust. J. Chem.* **2014**, *67*, 435−443.

(48) Chuang, Y.-Y.; Truhlar, D. G. Reaction-path dynamics with harmonic vibration frequencies in curvilinear internal coordinates: H + trans-$N_2H_2 \rightarrow N_2H + H_2$. *J. Chem. Phys.* **1997**, *107*, 83−89.

(49) Nguyen, K. A.; Jackels, C. F.; Truhlar, D. G. Reactionpath dynamics in curvilinear internal coordinates including torsions. *J. Chem. Phys.* **1996**, *104*, 6491−6496.

(50) Jackels, C. F.; Gu, Z.; Truhlar, D. G. Reactionpath potential and vibrational frequencies in terms of curvilinear internal coordinates. *J. Chem. Phys.* **1995**, *102*, 3188−3201.

(51) Decius, J. Compliance Matrix and Molecular Vibrations. *J. Chem. Phys.* **1963**, *38*, 241.

(52) Kraka, E.; Zou, W.; Filatov, M.; Gräfenstein, J.; Izotov, D.; Gauss, J.; He, Y.; Wu, A.; Polo, V.; Olsson, L. et al. *COLOGNE15*, 2015.

(53) Stoer, J.; Bulirsch, R. *Introduction to Numerical Analysis*; Springer: New York, 1980.

(54) Becke, A. D. Density-functional thermochemistry. III. The role of exact exchange. *J. Chem. Phys.* **1993**, *98*, 5648−5652.

(55) Stephens, P. J.; Devlin, F. J.; Chabalowski, C. F.; Frisch, M. J. Ab Initio Calculation of Vibrational Absorption and Circular Dichroism Spectra Using Density Functional Force Fields. *J. Phys. Chem.* **1994**, *98*, 11623−11627.

(56) Hariharan, P.; Pople, J. The influence of polarization functions on molecular orbital hydrogenation energies. *Theor. Chim. Acta* **1973**, *28*, 213−222.

(57) Andrae, D.; Haeusserman, U.; Dolg, M.; Stoll, H.; Preuss, H. Energy-adjusted ab initio pseudopotentials for the second and third row transition elements. *Theor. Chim. Acta* **1990**, *77*, 123−141.

(58) Cremer, D. In *Encyclopedia of Computational Chemistry*; Schleyer, P. v. R., Allinger, N. L., Clark, T., Gasteiger, J., Kollman, P. A., Schaefer, H. F., Schreiner, P. R., Eds.; Wiley: Chichester, UK, 1998; Vol. 3, p 1706.

(59) Cremer, D. In *Wiley Interdisciplinary's: Computational Molecular Science*; Schreiner, P. R., Allen, W., Eds.; Wiley: New York, 2011; Vol. *1*, pp 509−530.

(60) Raghavachari, K.; Trucks, G. W.; Pople, J. A.; Head-Gordon, M. A fifth-order perturbation comparison of electron correlation theories. *Chem. Phys. Lett.* **1989**, *157*, 479−483.

(61) Peterson, K.; Figgen, D.; Dolg, M.; Stoll, H. Energy-consistent relativistic pseudopotentials and correlation consistent basis sets for the 4d elements. *J. Chem. Phys.* **2007**, *126*, 124101−124111.

(62) Dunning, T., Jr. Gaussian basis sets for use in correlated molecular calculations. I. The atoms boron through neon and hydrogen. *J. Chem. Phys.* **1989**, *90*, 1007−1023.

(63) Wilson, A.; Mourik, T.; Dunning, T. J. Gaussian basis sets for use in correlated molecular calculations. VI. Sextuple zeta correlation consistent basis sets for boron through neon. *J. Mol. Struct.: THEOCHEM* **1997**, *388*, 339−349.

(64) Goerigk, L.; Grimme, S. A thorough benchmark of density functional methods for general main group thermochemistry, kinetics, and noncovalent interactions. *Phys. Chem. Chem. Phys.* **2011**, *13*, 6670−6688.

(65) Gräfenstein, J.; Cremer, D. Efficient DFT integrations by locally augmented radial grids. *J. Chem. Phys.* **2007**, *127*, 164113.

(66) Werner, H. J.; Knowles, P. J.; Kniza, G.; Manby, F. R.; Schütz, M. et al. *MOLPRO*, version 2010.1; a package of ab initio programs, 2010; see http://www.molpro.net.

(67) Stanton, J. F.; Gauss, J.; Harding, M. E.; Szalay, P. G.; Schütz, M. et al. *CFOUR*, a quantum chemical program package 2010; see http://www.cfour.de.

(68) Frisch, M. et al. *Gaussian 09*, revision A.1; Gaussian Inc.: Wallingford, CT, 2009.

(69) Hratchian, H. P.; Kraka, E. Improved Predictor-Corrector Integrators For Evaluating Reaction Path Curvature. *J. Chem. Theory Comput.* **2013**, *9*, 1481−1488.

(70) Hratchian, H. P.; Schlegel, H. B. Using Hessian updating to increase the efficiency of a Hessian based predictor-corrector reaction path following method. *J. Chem. Theory Comput.* **2005**, *1*, 61−69.

(71) Hratchian, H. P.; Frisch, M. J.; Schlegel, H. B. teepest descent reaction path integration using a first-order predictor-corrector method. *J. Chem. Phys.* **2010**, *133*, 224101.

(72) Hratchian, H. P.; Frisch, M. J. Integrating steepest-descent reaction pathways for large molecules. *J. Chem. Phys.* **2011**, *134*, 204103.

(73) Polyak, I.; Boulanger, E.; Sen, K.; Thiel, W. A microiterative intrinsic reaction coordinate method for large QM/MM systems. *Phys. Chem. Chem. Phys.* **2013**, *15*, 14188−14195.

(74) Sirca, S.; Horvat, M. *Computational Methods for Physicists*; Springer: New York, 2015; 335−374.

(75) Collins, M. A. Molecular Potential Potential Energy Surfaces for Chemical Reaction Dymanics. *Theor. Chem. Acc.* **2002**, *108*, 313−324.

(76) Ischtwan, J.; Collins, M. A. Molecular potential energy surfaces by interpolation. *J. Chem. Phys.* **1994**, *100*, 8080−8088.

(77) McIver, J. W., Jr.; Stanton, R. E. Symmetry Selection-Rules for Transition States. *J. Am. Chem. Soc.* **1972**, *94*, 8618−8620.

(78) Stanton, R. E.; McIver, J. W., Jr Group Theoretical Selection-Rules for Transition States of Chemical Reactions. *J. Am. Chem. Soc.* **1975**, *97*, 3632−3646.